


# SCIENTIFIC REPORTS



OPEN

## Anatase TiO<sub>2</sub> ultrathin nanobelts derived from room-temperature-synthesized titanates for fast and safe lithium storage

Received: 08 February 2015

Accepted: 05 June 2015

Published: 02 July 2015

Wei Wen<sup>1,3</sup>, Jin-ming Wu<sup>1</sup>, Yin-zhu Jiang<sup>1</sup>, Sheng-lan Yu<sup>1</sup>, Jun-qiang Bai<sup>1</sup>, Min-hua Cao<sup>2</sup> & Jie Cui<sup>4</sup>

Lithium-ion batteries (LIBs) are promising energy storage devices for portable electronics, electric vehicles, and power-grid applications. It is highly desirable yet challenging to develop a simple and scalable method for constructions of sustainable materials for fast and safe LIBs. Herein, we exploit a novel and scalable route to synthesize ultrathin nanobelts of anatase TiO<sub>2</sub>, which is resource abundant and is eligible for safe anodes in LIBs. The achieved ultrathin nanobelts demonstrate outstanding performances for lithium storage because of the unique nanoarchitecture and appropriate composition. Unlike conventional alkali-hydrothermal approaches to hydrogen titanates, the present room temperature alkaline-free wet chemistry strategy guarantees the ultrathin thickness for the resultant titanate nanobelts. The anatase TiO<sub>2</sub> ultrathin nanobelts were achieved simply by a subsequent calcination in air. The synthesis route is convenient for metal decoration and also for fabricating thin films of one/three dimensional arrays on various substrates at low temperatures, in absence of any seed layers.

The drastic depletion of traditional fossil energies and serious environmental pollutions stimulate tremendous research interests nowadays to develop sustainable energies and advanced energy-storage systems. Among various energy-storage systems, lithium-ion batteries (LIBs) are promising candidates for portable electronics, future electric vehicles/hybrid electric vehicles, and power-grid applications because of its high energy density<sup>1–3</sup>. The state-of-the-art anode material for LIBs, graphite, cannot fulfill the demands for large scale energy storage applications due to its poor rate performance and serious safety issues. Moreover, abundance, toxicity, synthetic methods and scalability of anode material should be considered to reduce the energy and environmental costs of LIBs<sup>3</sup>. Significant efforts have been made on Ti-based compounds, for example Li<sub>4</sub>Ti<sub>5</sub>O<sub>12</sub> and TiO<sub>2</sub>, as anodes for LIBs because of their **superior safety** as well as resource abundance and non-toxicity<sup>4–6</sup>. The inherent overcharge protection of Ti-based compounds arises from the fact that high Li-intercalation potential avoids the lithium dendrites and formation of the solid electrolyte inerphase (SEI) film as well. Also served as important functional material in photocatalysis<sup>7</sup>, energy conversion<sup>8</sup>, and gas sensors<sup>9</sup>, TiO<sub>2</sub> possesses a theoretical capacity of 335 mAhg<sup>-1</sup>, which is much higher than that of Li<sub>4</sub>Ti<sub>5</sub>O<sub>12</sub> (175 mAhg<sup>-1</sup>) having been successfully commercialized. Full cells constructed with TiO<sub>2</sub> and LiFePO<sub>4</sub> or LiNi<sub>0.5</sub>Mn<sub>1.5</sub>O<sub>4</sub> were reported to exhibit fascinating performances<sup>10</sup>. Among common TiO<sub>2</sub> polymorphs of anatase, rutile, and brookite, anatase

<sup>1</sup>State Key Laboratory of Silicon Materials, Key Laboratory of Advanced Materials and Applications for Batteries of Zhejiang Province, and School of Materials Science and Engineering, Zhejiang University, Hangzhou 310027, P. R. China. <sup>2</sup>Key Laboratory of Cluster Science, Ministry of Education of China, and Department of Chemistry, Beijing Institute of Technology, Beijing 100081, P. R. China. <sup>3</sup>College of Mechanical and Electrical Engineering, Hainan University, Haikou 570228, P. R. China. <sup>4</sup>Department of Physics, Wenzhou University, Wenzhou 325035, P. R. China. Correspondence and requests for materials should be addressed to J.-M.W. (email: msewjm@zju.edu.cn)

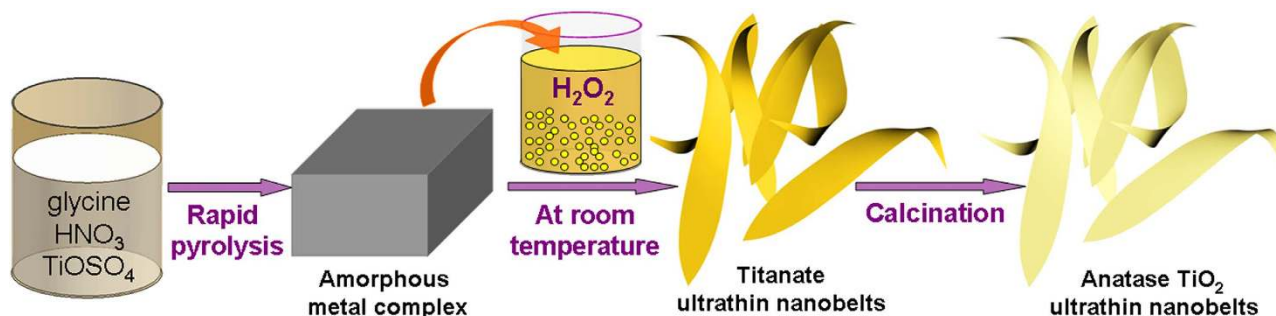


**Figure 1.** A schematic illustration showing the novel synthesis procedure of anatase TiO<sub>2</sub> ultrathin nanobelts. Firstly, an amorphous precursor was prepared via a rapid pyrolysis process. Then, room temperature treatment of the amorphous precursor with H<sub>2</sub>O<sub>2</sub> resulted in the formation of hydrogen titanate ultrathin nanobelts. Finally, anatase TiO<sub>2</sub> ultrathin nanobelts were obtained by a calcination of the hydrogen titanate ultrathin nanobelts.

presents the most excellent properties in lithium storage<sup>11</sup> and photocatalysis<sup>12</sup>. However, for lithium storage, anatase TiO<sub>2</sub> still suffers from low capacity and poor rate performance because of the sluggish Li ion diffusion and poor electronic conductivity<sup>11</sup>.

Reducing the dimension to a nanometer-scale range is one of the most effective strategies for anatase to improve the battery performance<sup>13–19</sup>, because the characteristic time constant  $t$  for diffusion is proportional to the square of the diffusion length  $L$  ( $t \approx L^2 D^{-1}$ )<sup>20</sup>. Specifically, two-dimensional (2D) nanomaterials can provide greatly increased electrolyte/electrode contact area and effectively shorten diffusion distance of Li ions, which in turn enhances their electrochemical performances<sup>21–23</sup>. For example, anatase TiO<sub>2</sub> nanosheets with exposed highly reactive (001) facets exhibited excellent properties for lithium storage<sup>24</sup>. Ultrathin 2D nanomaterials demonstrate many unique physical and chemical properties<sup>25</sup>. As a special nanostructure, nanobelts integrate the merits of 2D nanomaterials with enhanced charge transport that is characteristic of one-dimensional (1D) configuration.

Anatase TiO<sub>2</sub> nanobelts are typically fabricated via calcinations of hydrogen titanate, which is prepared by an alkaline hydrothermal treatment followed by a subsequent proton exchange<sup>26–29</sup>. Utilizing titanate derived by such a multi-step procedure as intermediates, TiO<sub>2</sub> with other 1D and 2D nanostructures could be obtained<sup>30–36</sup>. Recently, a vapour-phase hydrothermal method using ammonia instead of NaOH was developed for the direct growth of titanate nanotubes on a titanium substrate<sup>37</sup>. Mechanical agitation was also introduced into the alkaline hydrothermal technique to obtain elongated titanate nanotubes<sup>38</sup>. However, there are potential dangers in a high-pressure route, especially in large-scale productions, and even unfortunately, the anatase TiO<sub>2</sub> nanobelts by alkaline hydrothermal reactions usually exhibit a large thickness and low surface area<sup>26,27</sup>, which is not favored for the lithium storage. Certain low temperature techniques have been developed to synthesize titanate, including those with a nanosheet structure<sup>39</sup>; unfortunately, the sheet is still **not thin enough** and the specific surface area is also not high. It is still challenging to obtain TiO<sub>2</sub> with high performance for lithium storage via a simple and scalable synthesis method.

Herein, we present the synthesis of hydrogen titanate ultrathin nanobelts via a novel and robust H<sub>2</sub>O<sub>2</sub>-assisted wet-chemistry route at ambient conditions, as illustrated schematically in Fig. 1. An amorphous black Ti-based precursor was prepared via a rapid pyrolysis process, which, unlike common Ti-based precursor, is quite **water-proof** and hence easy to handle. Simply immersing the precursor in aqueous H<sub>2</sub>O<sub>2</sub> under the ambient conditions resulted in the formation of hydrogen titanate ultrathin nanobelts. With the morphology remained stable, the hydrogen titanate can be easily converted to anatase TiO<sub>2</sub> by a subsequent calcination at 400 °C in air. The resultant anatase nanobelts show excellent performances when utilized as anode for LIBs. The current strategy can be extended to prepare other ultrathin nanomaterials and gives hints to nanostructure design for electrode materials.

## Results

The formation of the hydrogen titanate ultrathin nanobelts is based on a dissolution/precipitation mechanism between H<sub>2</sub>O<sub>2</sub> and the Ti-based precursor. Hydrogen peroxide is inexpensive and environmentally benign, as the only degradation product of which is water. It is noted that many titanium precursors have been dissolved in aqueous H<sub>2</sub>O<sub>2</sub> solution to produce certain peroxo complexes<sup>40,41</sup>; however, synthesis of nanobelts in the presence of H<sub>2</sub>O<sub>2</sub> has not been reported yet<sup>42</sup>, let alone that of ultrathin nanobelts. Moreover, most titanium precursors, such as titanium alkoxides and titanium halides, are highly susceptible to water or even moisture. Once contacted with water, rapid hydrolysis occurs on the surface and TiO<sub>2</sub> is precipitated in the form of spherical nanoparticles rather than that of 1D or 2D nanostructures. Thus, a key technical issue herein is to explore a Ti-based precursor which does not hydrolyze in water.

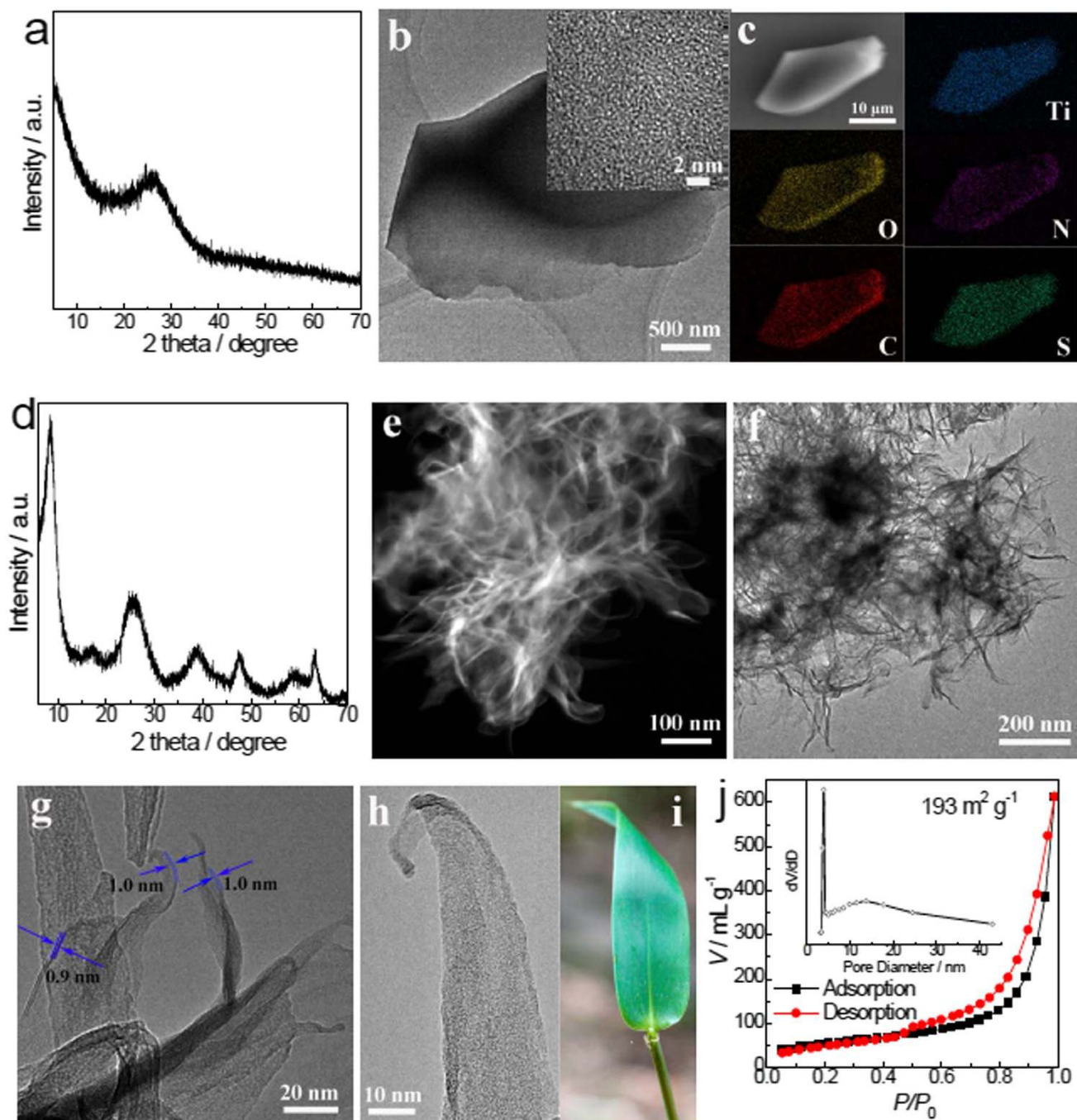


**Figure 2.** Characterization of precursor and titanate ultrathin nanobelts. (a) XRD pattern, (b) TEM image (inset: HRTEM image), and (c) EDS mapping of the precursor. (d) XRD pattern, (e) STEM image, (f, g) TEM images, and (h) HRTEM image of the as-prepared titanate ultrathin nanobelts. (i) Optical photograph of a bamboo leaf. (j) Nitrogen adsorption-desorption isotherm of the as-prepared titanate ultrathin nanobelts (inset: pore-size distribution calculated by BJH method from the desorption branch).

In current investigation, the black precursor achieved by the rapid pyrolysis is amorphous (Fig. 2a and Inset in Fig. 2b) and has a compact bulky morphology (Fig. 2b and Supplementary Fig. 1a), which remains almost unchanged after being immersed in water, either at ambient condition (Supplementary Fig. 1b) or at 160 °C in a hydrothermal condition (Supplementary Fig. 1c), demonstrating its excellent stability in water. This water-stable feature is very important for a convenient and safe usage and storage in practice. The precursor contains uniformly distributed Ti, O, N, C, and S elements (Fig. 2c). The mass fraction of C, N, and H measured by an element analysis (Flash EA 1112, ThermoFinnigan) is 25.2%, 15.4%, and 2.8%, respectively. The precursor mainly contains Ti-O, O-H, C-C, C-N, N-H,

O = C–O, Ti–S–O, and  $\text{SO}_4^{2-}$  species (Supplementary Fig. 2 and Supplementary Fig. 3). After the reaction with  $\text{H}_2\text{O}_2$  at ambient conditions, the precursor was converted to hydrogen titanate ultrathin nanobelts. Hydrogen titanates tend to form 2D morphologies because of their inherent lamellar structure. The room temperature synthesis further guarantees an ultrathin thickness of the titanate. Contrast to low yield of dominant liquid exfoliation route for preparation of ultrathin layered materials<sup>25</sup>, the precursor completely converts to hydrogen titanate ultrathin nanobelts in the present synthesis strategy. When compared with hydrothermal/solvothermal reactions widely adopted for the synthesis of most titanate nanostructures, the present route is energy-efficient as it demands no heating or external mechanical activations. The pyrolysis procedure for the precursor preparation is simple and rapid. The main external thermal energy input is for dehydration, which is the most time-consuming procedure. The pyrolysis process that finally achieved the black precursor is completed within just 2 min.

The phase and lamellar structures of the titanate were characterized by X-ray diffraction (XRD). All the diffraction peaks of the as-prepared sample (Fig. 2d) can be indexed to orthorhombic hydrogen titanate ( $\text{H}_2\text{Ti}_2\text{O}_5 \cdot \text{H}_2\text{O}$ , JCPDS card 47–0124). The broadening of the reflection peaks indicates small grains in the as-prepared titanate. The strong Bragg peak at  $2\theta = 8.5^\circ$  corresponds to the lamellar structure with an interlayer distance of ca. 1 nm. This interlayer distance is larger than that of hydrogen titanate ( $\text{H}_2\text{Ti}_2\text{O}_5 \cdot \text{H}_2\text{O}$ ), which may be attributed to the intercalation of nitrogen species and ammonium ions (Supplementary Fig. 4)<sup>37</sup>.

The as-prepared titanate exhibits a 1D-like architecture with abundant pores, as shown in the scanning transmission electron microscopy (STEM, Fig. 2e) and transmission electron microscopy (TEM, Fig. 2f) images. A closer observation reveals the nanobelt with a sharp tip (Fig. 2g,h), which looks like a bamboo leaf as a whole (Fig. 2i). The tips are curved and the edges are rolled up (Fig. 2e–h) because of the surface tension, which is commonly observed in graphene<sup>43,44</sup>. This suggests the ultrathin and flexible characteristics for the present titanate nanobelts. Many single-layered hydrogen titanates with a thickness of ca. 1 nm can be observed in Fig. 2g,h, which is in accordance with the XRD result. Some stacking nanobelts are also observed (Supplementary Fig. 5). The thickness of most nanobelts is estimated to be 1–2 nm (Fig. 2g,h, and Supplementary Fig. 5). The nanobelts sway, gather, shrink, and thicken under electron beam irradiation during TEM observations, which can be attributed to its ultrathin and flexible features and the instability of hydrogen titanate under the electron beam. It is previously observed that hydrogen titanate decomposed easily to anatase under focused electron beam irradiation<sup>45</sup>. This can explain the inconsistency that the titanate is crystallized as revealed by XRD (Fig. 2d) but shows no crystals in TEM observations (Fig. 2g,h). The titanate nanobelts possess a high specific surface area of  $193 \text{ cm}^3 \text{ g}^{-1}$  and large total pore volume of  $0.949 \text{ cm}^3 \text{ g}^{-1}$  (Fig. 2j). It is worth mentioning that the ultrathin nanobelts can be obtained in a wide range of  $\text{H}_2\text{O}_2$  amount (20–800 mL for one gram of precursor, Supplementary Fig. 6), which indicates a high reliability of the present synthesis strategy. The increased and then decreased Ti(IV) concentration in the solution (Supplementary Fig. 7) confirms a dissolution/precipitation mechanism for the formation of titanate nanobelts when immersing the black titanium-based precursor in aqueous  $\text{H}_2\text{O}_2$  solution.

Phase-pure anatase  $\text{TiO}_2$ , as verified by the XRD pattern (Fig. 3a) and Raman spectrum (Fig. 3b), can be obtained by a subsequent calcination of the as-prepared titanate in air, with the ultrathin nanobelts architecture well reserved (Fig. 3c–e). The transition temperature ( $400^\circ\text{C}$ ) from titanate to anatase here is lower than that of titanate obtained by hydrothermal reactions followed by a subsequent proton-exchange procedure<sup>26–30</sup>. Gentili et al. argued that a lower Na/Ti ratio in titanates was in favor of its transition to anatase<sup>46</sup>. Thus, the relatively low transition temperature could be attributed to the sodium-free feature for the titanate achieved in the current investigation. The high-resolution TEM (HRTEM) image of a nanobelt (Fig. 3f) exhibits a recognizable lattice spacing of 0.35 nm, corresponding to the (101) atomic plane of anatase  $\text{TiO}_2$ . The selected area electron diffraction (SAED) pattern (Inset in Fig. 3f) further confirms that the nanobelt is in anatase polycrystalline. The thickness of anatase nanobelts is typically below 5 nm (Fig. 3e), slightly larger than that of the as-synthesized titanate because of the phase transition and grain growth during the calcination in air. The specific surface area and total pore volume of the anatase  $\text{TiO}_2$  nanobelts is determined to be  $119 \text{ m}^2 \text{ g}^{-1}$  and  $0.666 \text{ cm}^3 \text{ g}^{-1}$  (Fig. 3g), respectively.

The electrochemical performance of the anatase  $\text{TiO}_2$  ultrathin nanobelts was evaluated in coin type lithium half-cells using Li foil as counter electrode and reference electrode at the room temperature. Based on the shape, the discharge curve of the  $\text{TiO}_2$  nanobelts (Fig. 4a) can be divided into three regions<sup>46</sup>: i) a voltage drop from the open circuit voltage to ca. 1.75 V, which is related to the formation of the solid–solution  $\text{Li}_x\text{TiO}_2$ ; ii) a voltage plateau at ca. 1.75 V, which indicates a phase equilibrium between the anorthorhombic  $\text{Li}_{0.5}\text{TiO}_2$  phase and the Li-poor tetragonal  $\text{Li}_x\text{TiO}_2$  phase; iii) a sloped region from 1.75 V to 1.0 V, which is attributed to the Li-ion insertion process into the surface layer of nano-sized  $\text{TiO}_2$  under the external force of the electric field. The high operating potential enables the batteries to be charged at high rates with high safety. The reaction in a  $\text{TiO}_2/\text{Li}$  half-cell is proposed to be,



Here, the maximum insertion coefficient  $x$  is determined to be only  $\sim 0.5$  (corresponding to a capacity of  $167.5 \text{ mAhg}^{-1}$ ) in bulk  $\text{TiO}_2$  due to the strong repulsive force between Li ions when the insertion ratio is greater than 0.5 [Refs 24,47]. Both theoretical simulations and experimental results demonstrated that

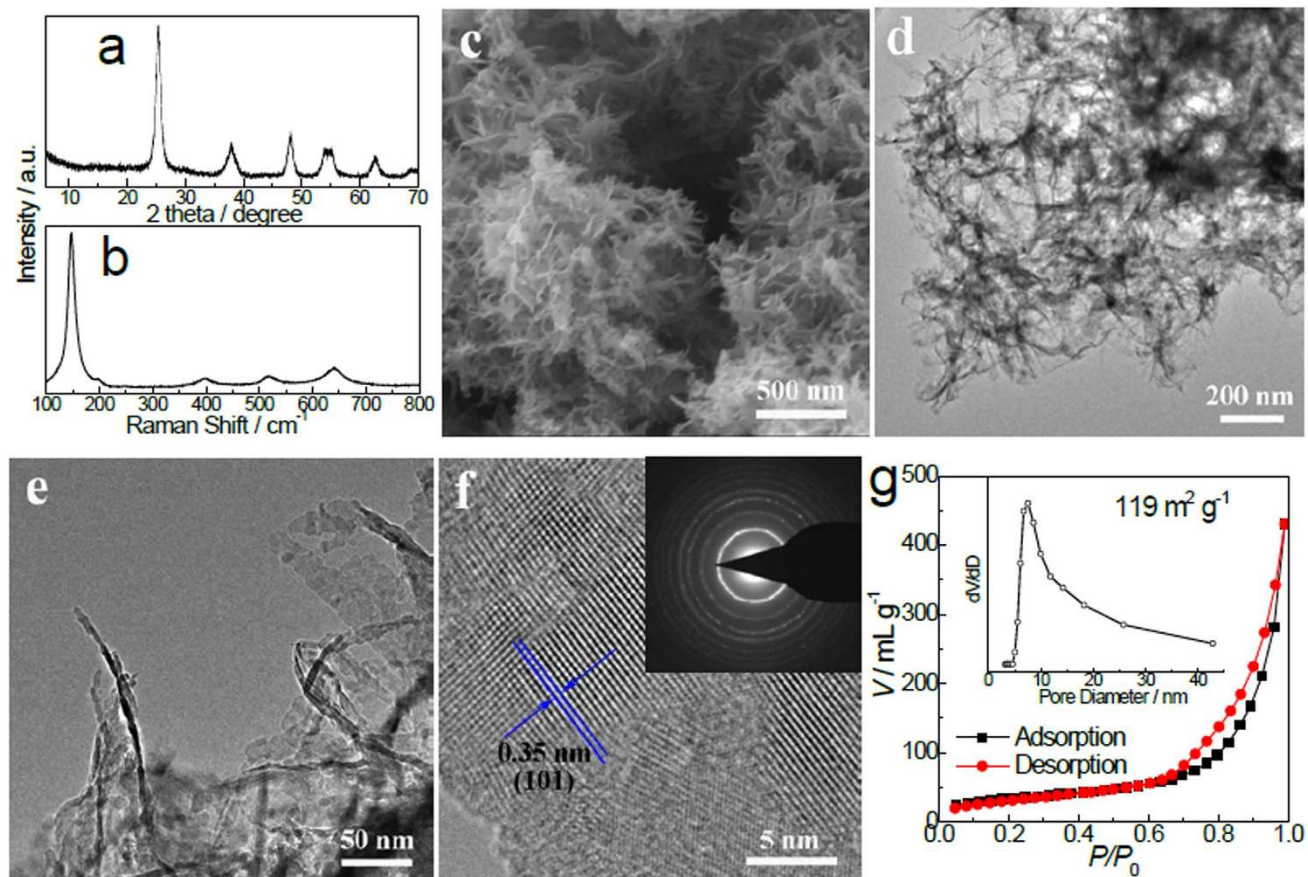


**Figure 3.** Characterization of anatase  $\text{TiO}_2$  ultrathin nanobelts. (a) XRD pattern. (b) Raman spectrum. (c) SEM image. (d,e) TEM images. (f) HRTEM image (inset: SAED pattern). (g) Nitrogen adsorption-desorption isotherm (inset: pore-size distribution calculated by BJH method from the desorption branch).

the theoretical capacity of titania-based electrodes can be dramatically improved when certain nanostructures were employed<sup>5,6,11</sup>. The nanobelts exhibit an enhanced specific capacity at 1 C ( $170 \text{ mAgh}^{-1}$ ) from 171 to  $197 \text{ mAgh}^{-1}$  when compared with Degussa P25, (a benchmark  $\text{TiO}_2$  nanoparticles) in the second cycle, as shown in Fig. 4a,b. Moreover, the nanobelts demonstrate an excellent cycling stability (Fig. 4b), which is much better than that of P25. The irreversible capacity in the 1st cycle is assigned to the non-reversible Li intercalation or the reaction between the electrolyte and the anatase surface<sup>13–19</sup>, which is common for most anode materials, especially for nanostructured materials. Fortunately, the irreversible capacity loss in the first cycle can be effectively and conveniently mitigated by a butyllithium ( $\text{C}_2\text{H}_5\text{OLi}$ ) treatment, or nano-sized Li powder incorporation<sup>48,49</sup>. After 5 cycles, the coulombic efficiency kept a stable value of over 99.5%, suggesting a highly reversible electrochemical reaction.

As shown in Fig. 4c, the anatase  $\text{TiO}_2$  ultrathin nanobelts deliver a discharge capacity of ca. 216, 204, 186, 164, 146, 126, and  $116 \text{ mAgh}^{-1}$  at a current rate of 0.5 C, 1 C, 2 C, 5 C, 10 C, 20 C, and 30 C, respectively. When the current is returned to 0.5 C, the anatase  $\text{TiO}_2$  ultrathin nanobelts resumes its capacity of  $204 \text{ mAgh}^{-1}$  after 80 cycles at different current densities, suggesting its excellent rate performance and good cycling stability. On the contrary, the P25 only displays 151, 112, 90, 65, 46, 33, and  $27 \text{ mAgh}^{-1}$  at 0.5 C, 1 C, 2 C, 5 C, 10 C, 20 C, and 30 C, respectively, which is much lower than that of the anatase  $\text{TiO}_2$  ultrathin nanobelts. It took only 2 min at 30 C to charge the nanobelts to  $116 \text{ mAgh}^{-1}$  while charging the P25 to  $112 \text{ mAgh}^{-1}$  took a much longer time of 1 h at 1 C (Fig. 4c). At 30 C, the nanobelts illustrate a 330% capacity improvement over the P25 (Fig. 4c). The electrochemical performance of anatase  $\text{TiO}_2$  ultrathin nanobelts is not only better than  $\text{TiO}_2$  nanobelts obtained by a common alkaline hydrothermal route<sup>50,51</sup> but also better than most of high performance  $\text{TiO}_2$  anodes<sup>17,19,24,52–58</sup>. The high electrochemical activity and low-cost preparation make the  $\text{TiO}_2$  ultrathin nanobelts a promising anode material for high performance and safe LIBs.

## Discussion

The excellent electrochemical performance is mainly ascribed to its unique nanostructure: a) the ultrathin thickness greatly shortens the diffusion distance of Li ions and the 1D-like structure possesses facile charge transport along the longitudinal dimension; b) the porous structure allows efficient

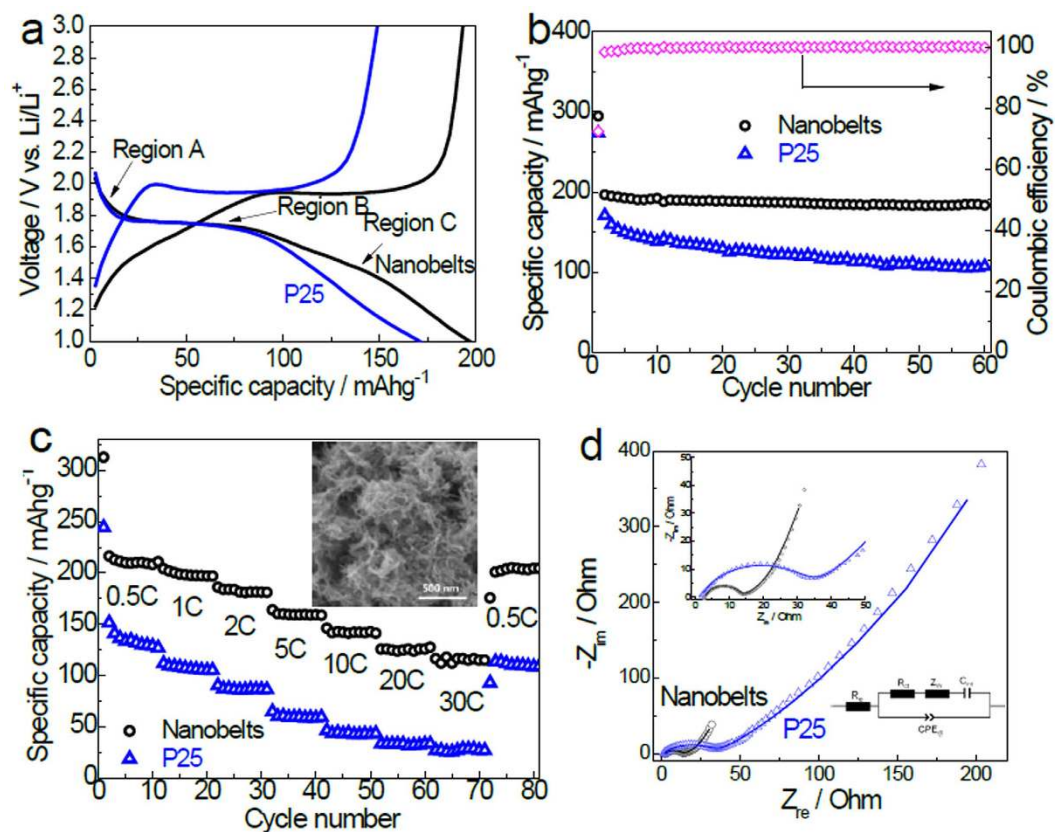


**Figure 4. Electrochemical measurements of the anatase TiO<sub>2</sub> ultrathin nanobelts and commercial P25 TiO<sub>2</sub> nanoparticles.** (a) The second discharge-charge profiles at the current rate of 1 C. (b) Cycling performance at 1 C. (c) Rate performance (inset: SEM image of the electrode after rate performance test). (d) Electrochemical impedance spectra measured in the open circuit potential over the frequency range from 100 kHz to 0.01 Hz (insets: enlarged view of the semicircle regions and the equivalent circuit), the specimens are those after the rate performance testing as illustrated in (c). The fitting results are represented by the solid lines.

ingress and infiltration of the electrolyte into the electrode, enabling a rapid ion transport, and provides abundant electrolyte/electrode contact area for charge transfer; c) the porous and flexible nanostructure effectively accommodates the volume/strain changes during the charge-discharge process. After the rate performance test for 80 cycles, the original ultrathin nanobelt structures can be well-retained (Inset in Fig. 4c), demonstrating the structure stability during charge-discharge cycles. The special composition of the nanobelts may also contribute to the excellent electrochemical performance. The X-ray photoelectron spectrum (XPS) N 1s signal ranging from 398 to 402 eV (Supplementary Fig. 8a) on the surface of the TiO<sub>2</sub> nanobelts can be attributed to major interstitial nitrogen (N<sub>inter</sub>) and minor chemically adsorbed nitrogen (N<sub>ad</sub>) species<sup>59</sup>. The S 2p peak at 168.4 eV (Supplementary Fig. 8b) is assigned to sulfur species in SO<sub>4</sub><sup>2-</sup> formed on the TiO<sub>2</sub> nanobelts surface<sup>59</sup>. The N and S are *in-situ* doped to TiO<sub>2</sub> nanobelts from the N-/S-containing precursor, resulting in a pale yellow color and an enhanced visible light absorption of the TiO<sub>2</sub> nanobelts (Supplementary Fig. 9). Recently, Jiao et al. reported that N and S co-doping could improve lithium storage capability of TiO<sub>2</sub><sup>59</sup>. The exact effect of surface species and crystal defects on lithium storage performance of the present TiO<sub>2</sub> nanobelts requires further investigations. Nevertheless, the nanobelts indeed show obviously enhanced charge transfer when compared with that of P25. In the electrochemical impedance spectroscopy (EIS) spectra illustrated in Fig. 4d, the intercept on  $Z_{\text{real}}$  axis in the high frequency region represents the resistance of electrolyte<sup>60</sup>. The depressed semicircle in the high-medium frequency region is assigned to the charge transfer process. The straight line at a lower frequency region represents the typical Warburg behavior, which is associated with the diffusion of Li ions in the electrodes. The impedance spectra are fitted to the proposed equivalent circuit (Inset in Fig. 4d), in which the equivalent circuit,  $R_e$ ,  $R_{ct}$ ,  $Z_w$ ,  $CPE_{dl}$ , and  $C_{int}$  represent the electrolyte resistance, the charge-transfer resistance, the Warburg impedance, the double-layer capacitance, and the intercalation capacitance, respectively<sup>61,62</sup>. The  $R_e$  of nanobelts and P25 is determined to be ca. 2.8  $\Omega$  and 1.9  $\Omega$ , respectively. The  $R_{ct}$  of nanobelts and P25 is determined to be ca. 10.5  $\Omega$  and 33.0  $\Omega$ , respectively. Although the electrolyte resistance of nanobelts is slightly larger than that of P25, the nanobelts show much smaller

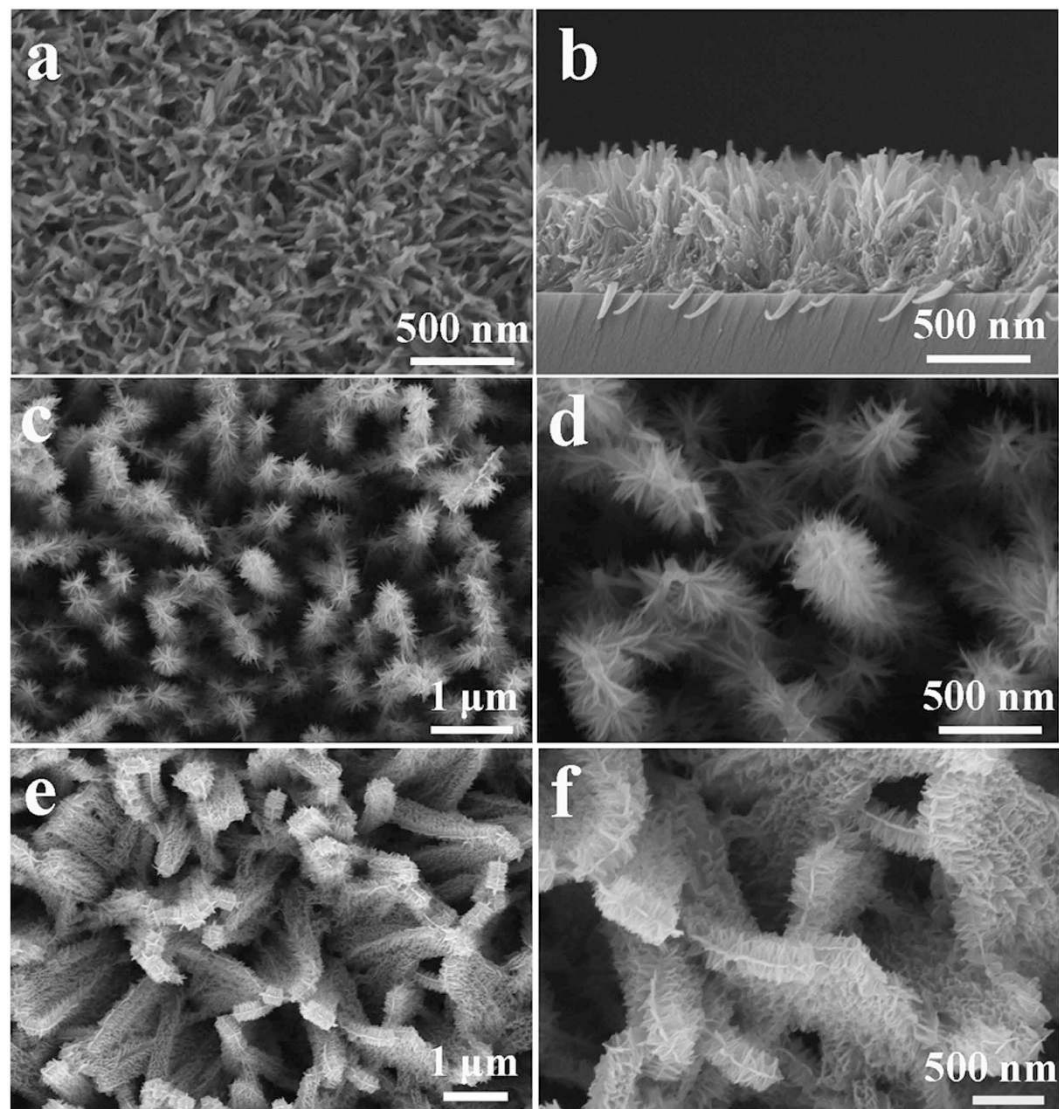


**Figure 5. Characterization of titanate array films.** (a) Top view and (b) cross sectional SEM images of titanate arrays precipitated on glass substrates. (c,d) SEM images of the core-shell branched nanowire arrays. (e,f) SEM images of the core-shell branched nanobelt arrays.

charge transfer resistance ( $R_{ct}$ ) than that of P25. The nanobelts have larger slopes and shorter lines in the low frequency region, implying a faster  $\text{Li}^+$  diffusion rates and smaller variation of diffusion paths<sup>63</sup>. Thus, the small charge-transfer resistance on the electrode/electrolyte interface and fast  $\text{Li}^+$  diffusion contribute to the excellent electrochemical performance of the ultrathin nanobelts<sup>62</sup>.

Interestingly, the synthesis strategy described here is capable of constructing titanate nanobelt arrays (Fig. 5a,b) and branched core-shell arrays (Fig. 5c–f, namely ultrathin nanobelts deposited on anatase  $\text{TiO}_2$  nanowire or nanobelt arrays) on various plane and complex substrates without the assistance of any seed layers.  $\text{TiO}_2$  arrays with various 1D/3D nanostructures have potential applications in regions of solar energy conversion, energy storage, and wettability control<sup>64–66</sup>. It is noted that the growth of nanostructured hydrogen titanate arrays via alkaline hydrothermal route is always limited to metallic Ti substrates<sup>32</sup>, or other substrates with a Ti coating<sup>35</sup>. Moreover, composition decoration can be conveniently achieved by this method (Supplementary Figs. 9–14), which may exhibit enhanced properties in lithium storage<sup>67</sup> and photoelectrochemical water splitting<sup>68,69</sup>.

In summary, hydrogen titanate ultrathin nanobelts were synthesized on a large scale at room temperature by a facile strategy based on a  $\text{H}_2\text{O}_2$ -assisted dissolution/precipitation process, with an appropriately designed water-proof Ti-based precursor. Anatase  $\text{TiO}_2$  can be obtained by a calcination of the as-synthesized titanate at a relatively low temperature of 400 °C in air, with the ultrathin nanobelts architecture well-reserved. The unique nanostructures and appropriate composition endowed the anatase  $\text{TiO}_2$  nanobelts excellent performances in lithium storage. The high electrochemical activity and low-cost preparation make the  $\text{TiO}_2$  ultrathin nanobelts a promising anode material for fast and safe LIBs. This

synthesis route is also convenient for metal decoration, as well as constructions of 1D/3D TiO<sub>2</sub> arrays on arbitrary substrates. The current strategy can be extended to prepare other ultrathin metal oxides, which may find wide applications in regions of catalysis, energy conversion, and energy storage.

## Methods

**Synthesis.** All reagents were of analytical grade and used as received without further purifications. 1.75 g glycine (C<sub>2</sub>H<sub>5</sub>NO<sub>2</sub>), 1.25 g titanium oxysulfate-sulfuric acid hydrate (Aladdin), and 0.6 mL nitric acid (65 wt. %) were added in 10 mL deionized water in a 100 mL crucible, which was transferred to a preheated furnace maintained at 400 °C for ca. 15 min to obtain a black precursor after ultrasounded for 10 min and stirred for 1 h. 0.5 g black precursor was then added into 400 mL H<sub>2</sub>O<sub>2</sub> (30 wt. %) and stored at room temperature for 72 h to obtain hydrogen titanates, which were converted to anatase TiO<sub>2</sub> counterparts after calcination in air at 400 °C for 1 h with a heating rate of 1 °C min<sup>-1</sup>.

**Characterizations.** X-ray diffraction (XRD) measurements were conducted on a XRD-6000 diffractometer (SHIMADZU) with a Cu K $\alpha$  radiation, operated at 40 kV, 40 mA ( $\lambda = 0.15406$  nm). The powder morphology was observed using a field emission scanning electron microscopy (FE-SEM, Hitachi S-4800, Tokyo, Japan, with EDS capabilities), together with a transmission electron microscopy (TEM, FEI-F20, FEI, USA) working at 200 kV. The X-ray photoelectron spectra (XPS) characterization was carried out on an Escalab 250Xi system (Thermo Fisher Scientific). The binding energy (BE) was calibrated by using the containment carbon (C 1s = 284.6 eV). The Raman spectra were taken on a LabRamHRUV (JDBin-yvon) Raman spectrometer, using the 514 nm line as the excitation source. The Brunauer-Emmett-Teller (BET) approach using adsorption data was utilized to determine the specific surface area. The sample was degassed at 150 °C for 14 h to remove physisorbed gases prior to the measurement. Titanium concentrations of the reaction solution sampled at various time intervals were measured by ICP-MS (XSENIES).

**Lithium storage test.** The working electrodes were prepared by a slurry coating procedure. The slurry consisted of 70 wt. % TiO<sub>2</sub> powders, 20 wt. % acetylene black, and 10 wt. % polyvinylidene fluoride (PVDF) dispersed in N-methyl pyrrolidinone (NMP), and was coated on a copper foil, which acted as a current collector. The film was dried at 90 °C for 20 h in vacuum. The cells were assembled in an argon-filled glove box using Li foil as a counter electrode and polypropylene (PP) film (Celgard 2300) as a separator. The electrolyte was 1 M LiPF<sub>6</sub> in a 50:50 (w/w) mixture of ethylene carbonate (EC) and diethyl carbonate (DEC). The charge-discharge tests were conducted on a LAND 2001A system. The electrochemical impedance spectroscopy (EIS) measurements were performed on a CHI660D electrochemical workstation.

## References

- Dunn, B., Kamath, H. & Tarascon, J. M. Electrical energy storage for the grid: A battery of choices. *Science* **334**, 928–935 (2011).
- Liu, N. *et al.* A pomegranate-inspired nanoscale design for large-volume-change lithium battery Anodes. *Nat. Nanotechnol.* **9**, 187–192 (2014).
- Larcher, D. & Tarascon, J. M. Towards greener and more sustainable batteries for electrical energy storage. *Nat. Chem.* **7**, 19–29 (2015).
- Feckl, J. M., Fominykh, K., Döblinger, M., Fattakhova-Rohlfing, D. & Bein, T. Nanoscale porous framework of lithium titanate for ultrafast lithium insertion. *Angew. Chem. Int. Ed.* **51**, 7459–7463 (2012).
- Chen, Z., Belharouak, I., Sun, Y. K. & Amine, K. Titanium-based anode materials for safe lithium-ion batteries. *Adv. Funct. Mater.* **23**, 959–969 (2013).
- Zhu, G. N., Wang, Y. G. & Xia, Y. Y. Ti-based compounds as anode materials for Li-ion batteries. *Energy Environ. Sci.* **5**, 6652–6667 (2012).
- Chen, X., Liu, L., Yu, P. Y. & Mao, S. S. Increasing solar absorption for photocatalysis with black hydrogenated titanium dioxide nanocrystals. *Science* **331**, 746–750 (2011).
- Crossland, E. J. W. *et al.* Mesoporous TiO<sub>2</sub> single crystals delivering enhanced mobility and optoelectronic device performance. *Nature* **495**, 215–230 (2013).
- Wang, Y. *et al.* Nanostructured sheets of Ti-O nanobelts for gas sensing and antibacterial applications. *Adv. Funct. Mater.* **18**, 1131–1137 (2008).
- Armstrong, G., Armstrong, A. R., Bruce, P. G., Reale, P. & Scrosati, B. TiO<sub>2</sub>(B) nanowires as an improved anode material for lithium-ion batteries containing LiFePO<sub>4</sub> or LiNi<sub>0.5</sub>Mn<sub>1.5</sub>O<sub>4</sub> cathodes and a polymer electrolyte. *Adv. Mater.* **18**, 2597–2600 (2006).
- Deng, D., Kim, M. G., Lee, J. Y. & Cho, J. Green energy storage materials: Nanostructured TiO<sub>2</sub> and Sn-based anodes for lithium-ion batteries. *Energy Environ. Sci.* **2**, 818–837 (2009).
- Chen, X. & Mao, S. S. Titanium dioxide nanomaterials: Synthesis, properties, modifications, and applications. *Chem. Rev.* **107**, 2891–2959 (2007).
- Ren, Y., Hardwick, L. J. & Bruce, P. G. Lithium intercalation into mesoporous anatase with an ordered 3D pore structure. *Angew. Chem. Int. Ed.* **49**, 2570–2574 (2010).
- Zhang, G., Wu, H. B., Song, T., Paik, U. & Lou, X. W. TiO<sub>2</sub> hollow spheres composed of highly crystalline nanocrystals exhibit superior lithium storage properties. *Angew. Chem. Int. Ed.* **53**, 12590–12593 (2014).
- Shin, J. Y., Samuelis, D. & Maier, J. Sustained lithium-storage performance of hierarchical, nanoporous anatase TiO<sub>2</sub> at high rates: Emphasis on interfacial storage phenomena. *Adv. Funct. Mater.* **21**, 3464–3472 (2011).
- Kim, S. W. *et al.* Fabrication and electrochemical characterization of TiO<sub>2</sub> three-dimensional nanonetwork based on peptide assembly. *ACS Nano* **3**, 1085–1090 (2009).
- Ye, J. *et al.* Nanoporous anatase TiO<sub>2</sub> mesocrystals: Additive-free synthesis, remarkable crystalline-phase stability, and improved lithium insertion behavior. *J. Am. Chem. Soc.* **133**, 933–940 (2011).
- Saravanan, K., Ananthanarayanan, K. & Balaya, P. Mesoporous TiO<sub>2</sub> with high packing density for superior lithium storage. *Energy Environ. Sci.* **3**, 939–948 (2010).



19. Tartaj, P. & Amarilla, J. M. Multifunctional response of anatase nanostructures based on 25 nm mesocrystal-like porous assemblies. *Adv. Mater.* **23**, 4904–4907 (2011).
20. Zhang, H., Yu, X. & Braun, P. V. Three-dimensional bicontinuous ultrafast-charge and -discharge bulk battery electrodes. *Nat. Nanotechnol.* **6**, 277–281 (2011).
21. Liu, J., Chen, J. S., Wei, X., Lou, X. W. & Liu, X. W. Sandwich-like, stacked ultrathin titanate nanosheets for ultrafast lithium storage. *Adv. Mater.* **23**, 998–1002 (2011).
22. Liu, S. *et al.* Nanosheet-constructed porous TiO<sub>2</sub>-B for advanced lithium ion batteries. *Adv. Mater.* **24**, 3201–3204 (2012).
23. Kim, G. *et al.* TiO<sub>2</sub> nanodisks designed for Li-ion batteries: A novel strategy for obtaining an ultrathin and high surface area anode material at the ice interface. *Energy Environ. Sci.* **6**, 2932–2938 (2013).
24. Chen, J. S. *et al.* Constructing hierarchical spheres from large ultrathin anatase TiO<sub>2</sub> nanosheets with nearly 100% exposed (001) facets for fast reversible lithium storage. *J. Am. Chem. Soc.* **132**, 6124–6130 (2010).
25. Zhang, X. & Xie, Y. Recent advances in free-standing two-dimensional crystals with atomic thickness: Design, assembly and transfer strategies. *Chem. Soc. Rev.* **42**, 8187–8199 (2013).
26. Wu, N. *et al.* Shape-enhanced photocatalytic activity of single-crystalline anatase TiO<sub>2</sub> (101) nanobelts. *J. Am. Chem. Soc.* **132**, 6679–6685 (2010).
27. Kiatkittipong, K., Scott, J. & Amal, R. Hydrothermally synthesized titanate nanostructures: Impact of heat treatment on particle characteristics and photocatalytic properties. *ACS Appl. Mater. Interfaces* **3**, 3988–3996 (2011).
28. Wang, J. *et al.* Origin of photocatalytic activity of nitrogen-doped TiO<sub>2</sub> nanobelts. *J. Am. Chem. Soc.* **131**, 12290–12297 (2009).
29. Zhou, W. *et al.* Synthesis of few-layer MoS<sub>2</sub> nanosheet-coated TiO<sub>2</sub> nanobelt heterostructures for enhanced photocatalytic activities. *Small* **9**, 140–147 (2013).
30. Yoshida, R., Suzuki, Y. & Yoshikawa, S. Syntheses of TiO<sub>2</sub>(B) nanowires and TiO<sub>2</sub> anatase nanowires by hydrothermal and post-heat treatments. *J. Solid State Chem.* **178**, 2179–2185 (2005).
31. Kasuga, T., Hiramatsu, M., Hoson, A., Sekino, T. & Niihara, K. Titania nanotubes prepared by chemical processing. *Adv. Mater.* **11**, 1307–1311 (1999).
32. Liao, J. Y. *et al.* Multifunctional TiO<sub>2</sub>-C/MnO<sub>2</sub> core-double-shell nanowire arrays as high-performance 3D electrodes for lithium ion batteries. *Nano Lett.* **13**, 5467–5473 (2013).
33. Li, W. *et al.* Hydrothermal etching assisted crystallization: A facile route to functional yolk-shell titanate microspheres with ultrathin nanosheets-assembled double shells. *J. Am. Chem. Soc.* **133**, 15830–15833 (2011).
34. Zhang, Y. *et al.* Three-dimensional CdS-titanate composite nanomaterials for enhanced visible-light-driven hydrogen evolution. *Small* **9**, 996–1002 (2013).
35. Miyauchi, M. & Tokudome, H. Super-hydrophilic and transparent thin films of TiO<sub>2</sub> nanotube arrays by a hydrothermal reaction. *J. Mater. Chem.* **17**, 2095–2100 (2007).
36. Bavykin, D. V., Friedrich, J. M. & Walsh, F. C. Protonated titanates and TiO<sub>2</sub> nanostructured materials: Synthesis, properties, and applications. *Adv. Mater.* **18**, 2807–2824 (2006).
37. Liu, P. *et al.* A facile vapor-phase hydrothermal method for direct growth of titanate nanotubes on a titanium substrate via a distinctive nanosheet roll-up mechanism. *J. Am. Chem. Soc.* **133**, 19032–19035 (2011).
38. Tang, Y. *et al.* Mechanical force-driven growth of elongated bending TiO<sub>2</sub>-based nanotubular materials for ultrafast rechargeable lithium ion batteries. *Adv. Mater.* **26**, 6111–6118 (2014).
39. Sutradhar, N., Sinhamahapatra, A., Pahari, S. K., Bajaj, H. C. & Panda, A. B. Room temperature synthesis of protonated layered titanate sheets using peroxy titanium carbonate complex solution. *Chem. Commun.* **47**, 7731–7733 (2011).
40. Wu, J. M. *et al.* Large-scale preparation of ordered titania nanorods with enhanced photocatalytic activity. *Langmuir* **21**, 6995–7002 (2005).
41. Tengvall, P., Elwing, H. & Lundstrom, I. Titanium gel made from metallic titanium and hydrogen peroxide. *J. Colloid Interf. Sci.* **130**, 405–413 (1989).
42. Piquemal, J. Y., Briot, E. & Brégeault, J. M. Preparation of materials in the presence of hydrogen peroxide: From discrete or “zero-dimensional” objects to bulk materials. *Dalton Trans.* **42**, 29–45 (2013).
43. Meyer, J. C. *et al.* The structure of suspended graphene sheets. *Nature* **446**, 60–63 (2007).
44. Ortolani, L. *et al.* Folded graphene membranes: Mapping curvature at the nanoscale. *Nano Lett.* **12**, 5207–2512 (2012).
45. Yang, H. G. & Zeng, H. C. Synthetic architectures of TiO<sub>2</sub>/H<sub>2</sub>Ti<sub>5</sub>O<sub>11</sub>·H<sub>2</sub>O, ZnO/H<sub>2</sub>Ti<sub>5</sub>O<sub>11</sub>·H<sub>2</sub>O, ZnO/TiO<sub>2</sub>/H<sub>2</sub>Ti<sub>5</sub>O<sub>11</sub>·H<sub>2</sub>O, and ZnO/TiO<sub>2</sub> nanocomposites. *J. Am. Chem. Soc.* **127**, 270–270 (2005).
46. Gentili, V. *et al.* Lithium insertion into anatase nanotubes. *Chem. Mater.* **24**, 4468–4476 (2012).
47. Kavan, L., Rathouský, J., Grätzel, M., Shklover, V. & Zukal, A. Surfactant-templated TiO<sub>2</sub> (anatase): Characteristic features of lithium insertion electrochemistry in organized nanostructures. *J. Phys. Chem. B* **104**, 12012–12020 (2000).
48. Brutti, S., Gentili, V., Menard, H., Scrosati, B. & Bruce, P. G. TiO<sub>2</sub>(-B) nanotubes as anodes for lithium batteries: Origin and mitigation of irreversible capacity. *Adv. Energy Mater.* **2**, 322–327 (2012).
49. Wang, X. L. *et al.* Amorphous hierarchical porous GeO<sub>x</sub> as high-capacity anodes for Li ion batteries with very long cycling life. *J. Am. Chem. Soc.* **133**, 20692–20695 (2011).
50. Gao, P. *et al.* Epitaxial growth route to crystalline TiO<sub>2</sub> nanobelts with optimizable electrochemical performance. *ACS Appl. Mater. Interfaces* **5**, 368–373 (2013).
51. Han, W. Q. & Wang, X. L. Carbon-coated Magnéli-phase Ti<sub>n</sub>O<sub>2n-1</sub> nanobelts as anodes for Li-ion batteries and hybrid electrochemical cells. *Appl. Phys. Lett.* **97**, 243104 (2010).
52. Hong, Z., Wei, M., Lan, T., Jiang, L. & Cao, G. Additive-free synthesis of unique TiO<sub>2</sub> mesocrystals with enhanced lithium-ion intercalation properties. *Energy Environ. Sci.* **5**, 5408–5413 (2012).
53. Yang, S., Feng, X. & Müllen, K. Sandwich-like, graphene-based titania nanosheets with high surface area for fast lithium storage. *Adv. Mater.* **23**, 3575–3579 (2011).
54. Li, W. *et al.* Sol-gel design strategy for ultradispersed TiO<sub>2</sub> nanoparticles on graphene for high-performance lithium ion batteries. *J. Am. Chem. Soc.* **135**, 18300–18303 (2013).
55. Qiu, B., Xing, M. & Zhang, J. Mesoporous TiO<sub>2</sub> nanocrystals grown *in situ* on graphene aerogels for high photocatalysis and lithium-ion Batteries. *J. Am. Chem. Soc.* **136**, 5852–5855 (2014).
56. Han, H. *et al.* Nitridated TiO<sub>2</sub> hollow nanofibers as an anode material for high power lithium ion batteries. *Energy Environ. Sci.* **4**, 4532–4536 (2011).
57. Guo, Y. G., Hu, Y. S., Sigle, W. & Maier, J. Superior electrode performance of nanostructured mesoporous TiO<sub>2</sub> (Anatase) through efficient hierarchical mixed conducting networks. *Adv. Mater.* **19**, 2087–2091 (2007).
58. Xia, T., Zhang, W., Murowchick, J. B., Liu, G. & Chen, X. A facile method to improve the photocatalytic and lithium-ion rechargeable battery performance of TiO<sub>2</sub> nanocrystals. *Adv. Energy Mater.* **3**, 1516–1523 (2013).
59. Jiao, W. *et al.* High-rate lithium storage of anatase TiO<sub>2</sub> crystals doped with both nitrogen and sulfur. *Chem. Commun.* **49**, 3461–3463 (2013).
60. Xiao, Y., Zeng, L. & Cao, M. Hybridization and pore engineering for achieving high-performance lithium storage of carbide as anode material. *Nano Energy* **12**, 152–160 (2015).

61. Kim, M. S. *et al.* Ultra-high Li storage capacity achieved by hollow carbon capsules with hierarchical nanoarchitecture. *J. Mater. Chem.* **21**, 19362–19367 (2011).
62. Giannuzzi, R. *et al.* Ultrathin TiO<sub>2</sub>(B) nanorods with superior lithium-ion storage performances. *ACS Appl. Mater. Interfaces* **6**, 1933–1943 (2014).
63. Wu, H., Xu, M., Wang, Y. & Zheng, G. Branched Co<sub>3</sub>O<sub>4</sub>/Fe<sub>2</sub>O<sub>3</sub> nanowires as high capacity lithium-ion battery anodes. *Nano Res.* **6**, 167–173 (2013).
64. Yang, X. *et al.* Hierarchically nanostructured rutile arrays: acid vapor oxidation growth and tunable morphologies. *ACS Nano* **3**, 1212–1218 (2009).
65. Cho, I. S. *et al.* Branched TiO<sub>2</sub> nanorods for photoelectrochemical hydrogen production. *Nano Lett.* **11**, 4978–4984 (2011).
66. Wu, W. Q. *et al.* Maximizing omnidirectional light harvesting in metal oxide hyperbranched array architectures. *Nat. Commun.* **5**, 3968 (2014).
67. Wang, Y., Smarsly, B. M. & Djerdj, I. Niobium doped TiO<sub>2</sub> with mesoporosity and its application for lithium insertion. *Chem. Mater.* **22**, 6624–6631 (2010).
68. Liu, B. *et al.* Large-scale synthesis of transition-metal-doped TiO<sub>2</sub> nanowires with controllable overpotential. *J. Am. Chem. Soc.* **135**, 9995–9998 (2013).
69. Cho, I. S. *et al.* Codoping titanium dioxide nanowires with tungsten and carbon for enhanced photoelectrochemical performance. *Nat. Commun.* **4**, 1723 (2013).

## Acknowledgments

This work is support by Zhejiang Provincial Natural Science Foundation of China under Grant No. LY13E020001. Dr Wen thanks a scholarship award for Excellent Doctoral Student granted by Ministry of Education, China for the financial support.

## Author Contributions

W.W. and J.M.W. conceived the concept and experiments. W.W. carried out the materials synthesis and part of materials characterizations and part of electrochemical measurements. J.Q.B. participated in part of the materials synthesis. Y.Z.J., S.L.Y., M.H.C. and J.C. participated in part of the materials characterizations and electrochemical measurements. W.W. and J.M.W. co-wrote the paper. All authors discussed the results and commented on the manuscript.

## Additional Information

**Supplementary information** accompanies this paper at <http://www.nature.com/srep>

**Competing financial interests:** The authors declare no competing financial interests.

**How to cite this article:** Wen, W. *et al.* Anatase TiO<sub>2</sub> ultrathin nanobelts derived from room-temperature-synthesized titanates for fast and safe lithium storage. *Sci. Rep.* **5**, 11804; doi: 10.1038/srep11804 (2015).



This work is licensed under a Creative Commons Attribution 4.0 International License. The images or other third party material in this article are included in the article's Creative Commons license, unless indicated otherwise in the credit line; if the material is not included under the Creative Commons license, users will need to obtain permission from the license holder to reproduce the material. To view a copy of this license, visit <http://creativecommons.org/licenses/by/4.0/>